

A reappraisal of the wrong-sign $hb\bar{b}$ coupling and the study of $h \rightarrow Z\gamma$

Duarte Fontes,^{1,*} J. C. Romão,^{1,†} and João P. Silva^{2,1,‡}

¹*Centro de Física Teórica de Partículas (CFTP), Instituto Superior Técnico,
Universidade de Lisboa, 1049-001 Lisboa, Portugal*

²*Instituto Superior de Engenharia de Lisboa - ISEL, 1959-007 Lisboa, Portugal*
(Dated: June 25, 2014)

It has been pointed out recently that current experiments still allow for a two Higgs doublet model where the $hb\bar{b}$ coupling ($k_D m_b/v$) is negative; a sign opposite to that of the Standard Model. Due to the importance of delayed decoupling in the hH^+H^- coupling, $h \rightarrow \gamma\gamma$ improved measurements will have a strong impact on this issue. For the same reason, measurements or even bounds on $h \rightarrow Z\gamma$ are potentially interesting. In this article, we revisit this problem, highlighting the crucial importance of $h \rightarrow VV$, which can be understood with simple arguments. We show that the impacts on $k_D < 0$ models of both $h \rightarrow b\bar{b}$ and $h \rightarrow \tau^+\tau^-$ are very sensitive to input values for the gluon fusion production mechanism; in contrast, $h \rightarrow \gamma\gamma$ and $h \rightarrow Z\gamma$ are not. We also inquire if the search for $h \rightarrow Z\gamma$ and its interplay with $h \rightarrow \gamma\gamma$ will impact the sign of the $hb\bar{b}$ coupling. Finally, we study these issues in the context of the Flipped two Higgs doublet model.

PACS numbers: 12.60.Fr, 14.80.Ec, 14.80.-j

I. INTRODUCTION

After the discovery of the Higgs particle by the ATLAS [1] and CMS [2] experiments at LHC [3], it became critically important to check how close its features are to those in the Standard Model (SM). Recently, it has been emphasized by Carmi *et al.* [4], by Chiang and Yagyu [5], by Santos [6] and by Ferreira *et al.* [7] that current data are consistent with a lightest Higgs from a two Higgs doublet model (2HDM) with a softly-broken Z_2 symmetry and CP conservation, where the coupling of the bottom quark to the Higgs ($k_D m_b/v$) has a sign *opposite* to that in the SM.

Besides the SM gauge and fermion sector, the model has two CP-even scalars, h and H , one CP-odd scalar A , and a conjugate pair of charged scalars H^\pm . The scalar potential can be written in terms of the usual vacuum expectation value (vev) $v = 246$ GeV, and seven parameters: the four masses, $m_h, m_H > m_h, m_A$, and m_{H^\pm} ; two mixing angles, α and β , and the (real) quadratic term breaking Z_2 , m_{12}^2 . With a suitable basis choice, $\beta > 0$ and $-\pi/2 \leq \alpha \leq \pi/2$. Details about this model can be found, for instances, in Refs. [8, 9]. We follow here the notation of the latter.

We concentrate on the Type II 2HDM, where the fermion couplings with the lightest Higgs are (multiplied by the mass of the appropriate fermion and divided by v)

$$k_U = \frac{\cos \alpha}{\sin \beta}, \quad (1)$$

for the up-type quarks, and

$$k_D = -\frac{\sin \alpha}{\cos \beta}, \quad (2)$$

for both the down-type quarks and the charged leptons. In the SM limit, $k_U = k_D = 1$. Thus, $\sin \alpha$ negative (positive) corresponds to the (opposite of the) SM sign. The couplings of h to vector boson pairs are

$$g_{hVV} = k_V g_{hVV}^{\text{SM}} = \sin(\beta - \alpha) g_{hVV}^{\text{SM}}, \quad (3)$$

where $VV = ZZ, W^+W^-$, and the coupling to a pair of charged Higgs bosons may be written as [10]

$$g_{hH^+H^-} = -\frac{2m_{H^\pm}^2}{v} (g_1 + g_2 + g_3), \quad (4)$$

*E-mail: duartefontes@tecnico.ulisboa.pt

†E-mail: jorge.romao@tecnico.ulisboa.pt

‡E-mail: jpsilva@cftp.tecnico.ulisboa.pt

where

$$\begin{aligned}
g_1 &= \sin(\beta - \alpha) \left(1 - \frac{m_h^2}{2m_{H^\pm}^2} \right), \\
g_2 &= \frac{\cos(\beta + \alpha)}{\sin(2\beta)} \frac{m_h^2}{m_{H^\pm}^2}, \\
g_3 &= -\frac{2\cos(\beta + \alpha)}{\sin^2(2\beta)} \frac{m_{12}^2}{m_{H^\pm}^2}.
\end{aligned} \tag{5}$$

We have checked, with the help of `FeynRules` [11], that this expression is correct.

Before H^\pm are detected directly, their effect might be detected indirectly through loop contributions involving $g_{hH^\pm H^\pm}$, especially in decays of h which are already loop decays in the SM, such as $h \rightarrow \gamma\gamma$ and $h \rightarrow Z\gamma$. This is possible if $m_{H^\pm} \sim v$, because there will be a light particle in the loop. This is also possible for $m_{H^\pm} \gg v$, when the H^\pm loop contribution approaches a constant [12, 13]. However, making m_{H^\pm} too large will require quartic couplings in violation of the unitarity bounds. This still leaves a rather wide range of H^\pm masses where the charged Higgs contributions to $h \rightarrow \gamma\gamma$ and $h \rightarrow Z\gamma$ could be detected. In Ref. [7], it is shown that such non-decoupling is unavoidable in $h \rightarrow \gamma\gamma$, if the wrong-sign $hb\bar{b}$ ($k_D < 0$) case is to conform to all current data. We have checked that such non-decoupling will also have an impact on $h \rightarrow Z\gamma$.

Our article is organized as follows. In Section II, we discuss our fit procedure. There are differences with respect to Ref. [7], most notably in the production rates, as shown in section II A. In section II B, we point out the crucial importance of the VV channel by itself, which can be understood with quite simple arguments. It turns out that, once VV is constrained, $b\bar{b}$ and $\tau^+\tau^-$ are rather sensitive to the production rates, while $\gamma\gamma$ and $Z\gamma$ are not. This feature is explained in detail in section II C. Section III includes our predictions for the next LHC run, which will occur at 14 TeV (not 8 TeV). We show that, before applying the constraints on VV , $Z\gamma$ can be above the SM value by a factor of two. If such values were to be measured, we would exclude the SM. However, $Z\gamma$ can also take the SM value, and it cannot be used to exclude $k_D < 0$. In section IV, we analyze the Flipped 2HDM, where the coupling to the charged leptons goes like k_U in Eq. (1) – not like k_D in Eq. (2). We draw our conclusions in Section V.

II. FIT PROCEDURE AND SOME RESULTS

The scalar particle found at the LHC has been seen in the $\gamma\gamma$, ZZ^* , WW^* , and $\tau^+\tau^-$ final states, with errors of order 20%. The $b\bar{b}$ final state is only seen (at LHC and the Tevatron) in the associated Vh production mechanism, with errors of order 50% [14, 15]. Searches have also been performed for the $Z\gamma$ final state [16, 17], with upper bounds around ten times the SM expectation at the 95% confidence level. Current LHC results can be found in Ref. [3].

These results for the $pp \rightarrow h \rightarrow f$ rates (where f is some final state) are usually presented in the form of ratios of observed rates to SM expectations. This is what we use to constrain the ratios between the 2HDM and SM rates

$$\mu_f = R_P R_D R_{TW}, \tag{6}$$

where the sub-indices P , D , and TW stand for “production”, “decay”, and “total width”, respectively. Here,

$$\begin{aligned}
R_P &= \frac{\sigma^{2\text{HDM}}(pp \rightarrow h)}{\sigma^{\text{SM}}(pp \rightarrow h)}, \\
R_D &= \frac{\Gamma^{2\text{HDM}}[h \rightarrow f]}{\Gamma^{\text{SM}}[h \rightarrow f]}, \\
R_{TW} &= \frac{\Gamma^{\text{SM}}[h \rightarrow \text{all}]}{\Gamma^{2\text{HDM}}[h \rightarrow \text{all}]},
\end{aligned} \tag{7}$$

where σ is the Higgs production mechanism, $\Gamma[h \rightarrow f]$ the decay width into the final state f , and $\Gamma[h \rightarrow \text{all}]$ is the total Higgs decay width.

We follow the strategy of Ref. [7], and assume that all observed decays have been measured at the SM rates, with the same error 20%. For the most part, we keep $b\bar{b}$ out of the mix, because: it has larger errors; it is only measured in the Vh production channel; and, as we will show, it is not needed in Type II models, where $\tau^+\tau^-$ has the same effect (which, moreover, is not very large). We will only assume that all production mechanisms are involved in $b\bar{b}$ and that its errors are of order 20% when we wish to compare with Ref. [7], explaining the differences in production.

We have performed extensive simulations of the type II 2HDM, with the usual strategy. We set $m_h = 125$ GeV, generate random points for $-\pi/2 \leq \alpha \leq \pi/2$, $1 \leq \tan \beta \leq 30$, $90 \text{ GeV} \leq m_A \leq 900 \text{ GeV}$, $125 \text{ GeV} \leq m_H \leq 900 \text{ GeV}$, $-(900 \text{ GeV})^2 \leq m_{12}^2 \leq (900 \text{ GeV})^2$, and $340 \text{ GeV} \leq m_{H^\pm} \leq 900 \text{ GeV}$. These coincide with the ranges in Ref. [7], where $\tan \beta$ and m_{H^\pm} were chosen to conform with B Physics and $Z \rightarrow b\bar{b}$ data.

For each point, we derive the parameters of the scalar potential, and we keep only those points which provide a bounded from below solution [18], respecting perturbative unitarity [19–21], and the constraints from the oblique radiative parameters S, T, U [22, 23]. At the end of this procedure, we have a set of possible 2HDM parameters, henceforth denoted simply by SET.

Next, we generate the rates for all channels, including all production mechanisms: $gg \rightarrow h$ (gluon fusion) at NNLO from HIGLU [24], $b\bar{b} \rightarrow h$ at NNLO from SusHi [25], Vh associated production, $t\bar{t}h$, and $VV \rightarrow h$ (vector boson fusion) [26]. In the SM, the production cross section is dominated by the gluon fusion process with internal top quark. Generically speaking, this also holds in the Type II 2HDM, but, given Eq. (2), the contribution from the gluon fusion process with internal bottom quark becomes more important as $\tan \beta$ increases.

A. Comparing with previous results

We start by requiring that all points in the SET obey $k_D < 0$ and $0.8 \leq \mu_f \leq 1.2$ for the VV , $\tau^+\tau^-$, $b\bar{b}$, and $\gamma\gamma$ at 8 GeV. The surviving points are plotted as a function of $\tan \beta$ in the left panel of Fig. 1, where we show the possible values of $\mu_{\gamma\gamma}$ (in black) and $\mu_{b\bar{b}}$ (in red/dark-gray). We notice that, although $\mu_{b\bar{b}}$ is in general larger than $\mu_{\gamma\gamma}$, the two regions overlap and, at the level of deviations of 20% from the SM, both are compatible with the SM value of one. We now assume that $h \rightarrow VV$ is measured within 5% of the SM: $0.95 \leq \mu_{VV} \leq 1.05$. The result is plotted in the right panel of Fig. 1. We found that $\mu_{\gamma\gamma}$ agrees, within errors, with that shown in Fig. 5-Left of Ref. [7], while our result for $\mu_{b\bar{b}}$ is well above theirs, which we also show in Fig. 1 (in cyan/light-gray). This is puzzling, since we can

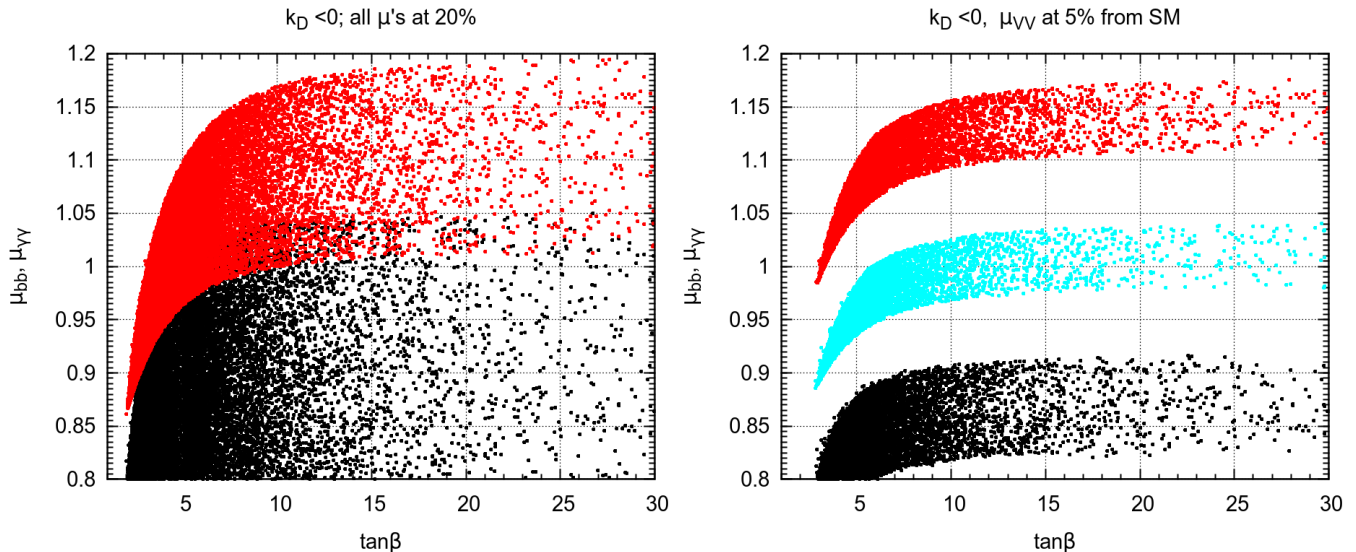


FIG. 1: Left panel: Assuming that all μ_f are within 20% of the SM prediction we plot $\mu_{b\bar{b}}$ (red/dark-gray) and $\mu_{\gamma\gamma}$ (black). Right panel: Assuming now that μ_{VV} are within 5% of the SM prediction we plot the same quantities. For comparison we also plot $\mu_{b\bar{b}}$ (cyan/light-gray) for the assumed production of Ref. [7].

reproduce their remaining plots.

After comparing notes with R. Santos from Ref. [7], we found that the difference originates in the gluon fusion production rates, because we are using values from an more recent version of HIGLU [24], and, eventually, different PDF's and energy scales. For example, they quote

$$\frac{\sigma(gg \rightarrow h)_{\text{NNLO}}^{2\text{HDM}}}{\sigma(gg \rightarrow h_{\text{SM}})_{\text{NNLO}}} = 1.06 \quad [\sin(\beta + \alpha) = 1], \quad (8)$$

while we, using the latest version (4.0) of HIGLU [24], obtain

$$\frac{\sigma(gg \rightarrow h)_{\text{NNLO}}^{2\text{HDM}}}{\sigma(gg \rightarrow h_{\text{SM}})_{\text{NNLO}}} = 1.126 \quad [\sin(\beta + \alpha) = 1]. \quad (9)$$

This apparently explains why our $\mu_{b\bar{b}}$ result (in red/dark-gray) lies above the one which we obtain (in cyan/light-gray) with the assumed production rates used in Ref. [7].

But, this raises another puzzle. If the only difference lies in the production rates, why do our results for $\mu_{\gamma\gamma}$ agree with those in Ref. [7]? This is what we turn to in section II C.

B. The crucial importance of $h \rightarrow VV$ and trigonometry

In the previous section, we required that all points obey $0.8 \leq \mu_f \leq 1.2$ for all final states VV , $\tau^+\tau^-$, $b\bar{b}$, and $\gamma\gamma$, simultaneously. The problem with this procedure is that one misses out on the crucial importance that μ_{VV} has on its own.

In this section, we only assume that $0.8 \leq \mu_{VV} \leq 1.2$, and we will make the cavalier assumption that the production is due exclusively to the gluon fusion with intermediate top, while the decay is due exclusively to the decay $h \rightarrow b\bar{b}$ [27]. Under these assumptions,

$$\mu_{VV} \approx \frac{k_U^2}{k_D^2} \sin^2(\beta - \alpha). \quad (10)$$

We now perform a simple trigonometric exercise. We vary α between $-\pi/2$ and $\pi/2$, $\tan\beta$ between 1 and 30, and we only keep those regions where $0.8 \leq \mu_{VV} \leq 1.2$, with the approximation in Eq. (10).

In Fig. 2, we show the remaining points in the $\sin\alpha - \tan\beta$ plane. This matches remarkably well the Fig. 2-Left

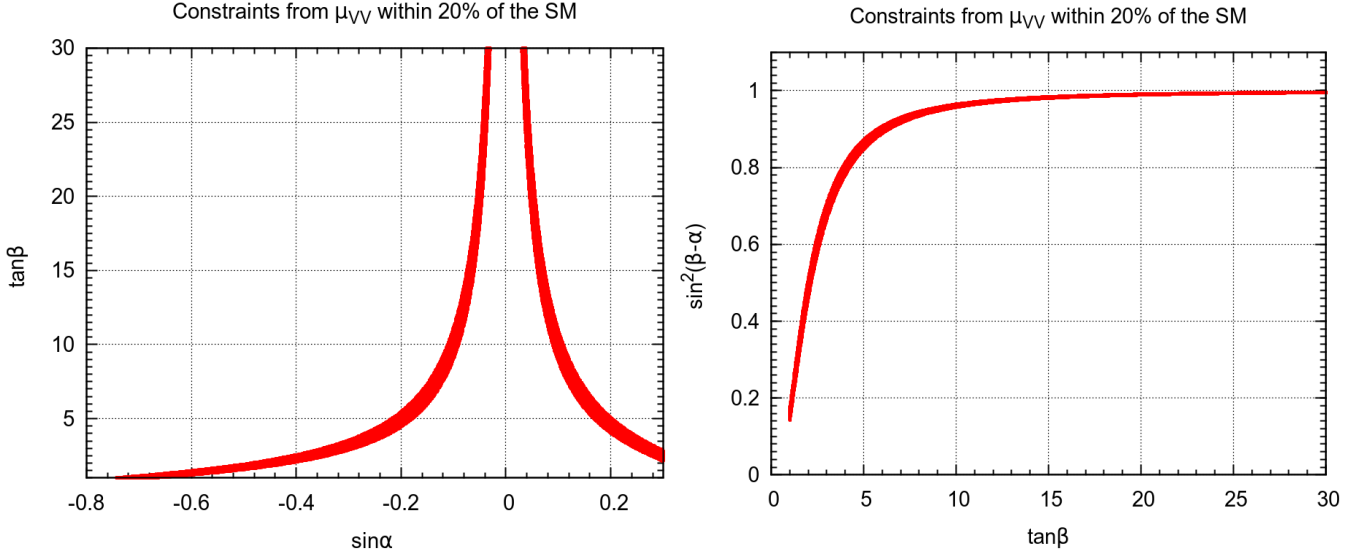


FIG. 2: Left panel: Plot of $\tan\beta$ as a function of $\sin\alpha$ for all the points that obey Eq. (10) with $0.8 \leq \mu_{VV} \leq 1.2$. Right panel: Plot of $\sin^2(\beta - \alpha)$ as a function of $\tan\beta$ for the points that obey Eq. (10) with $0.8 \leq \mu_{VV} \leq 1.2$ and have $k_D < 0$.

from Ref. [7]. That is, a simple back of the envelope calculation has most of the Physics. The left branch of the left panel of Fig. 2 corresponds to the SM sign ($k_D > 0$), and it lies very close to the curve $\sin(\beta - \alpha) = 1$. The right branch of the same figure corresponds to the wrong sign ($k_D < 0$), and lies very close to the curve $\sin(\beta + \alpha) = 1$ [6].

Under the same assumptions, we can draw $\sin^2(\beta - \alpha)$ as a function of $\tan\beta$, as seen in the right panel of Fig. 2, keeping only $\sin\alpha > 0$ ($k_D < 0$) points. Notice that $\sin^2(\beta - \alpha)$ becomes almost univocally defined in terms of $\tan\beta$. Indeed, fixing $\tan\beta$, and defining the fractional variation of $\sin^2(\beta - \alpha)$ around its average value by

$$\Delta = \frac{\sin^2(\beta - \alpha)_{\max} - \sin^2(\beta - \alpha)_{\min}}{\sin^2(\beta - \alpha)_{\max} + \sin^2(\beta - \alpha)_{\min}}, \quad (11)$$

we obtain the results in Fig. 3. For small $\tan\beta$, $\sin^2(\beta - \alpha)$ is determined to better than 10%, when μ_{VV} is fixed only to 20% accuracy. Although it might seem from Eq. (10) that it should be roughly the same, it turns out that the inclusion in Eq. (10) of k_U and k_D from Eqs. (1)-(2) helps in reducing the error. But things get even more accurate as $\tan\beta$ increases. For example, for $\tan\beta = 10$, $\sin^2(\beta - \alpha)$ differs very little from unity, and it is even more precisely defined around its average value; an accuracy better than 0.5%, coming from a μ_{VV} fixed only to 20% accuracy.

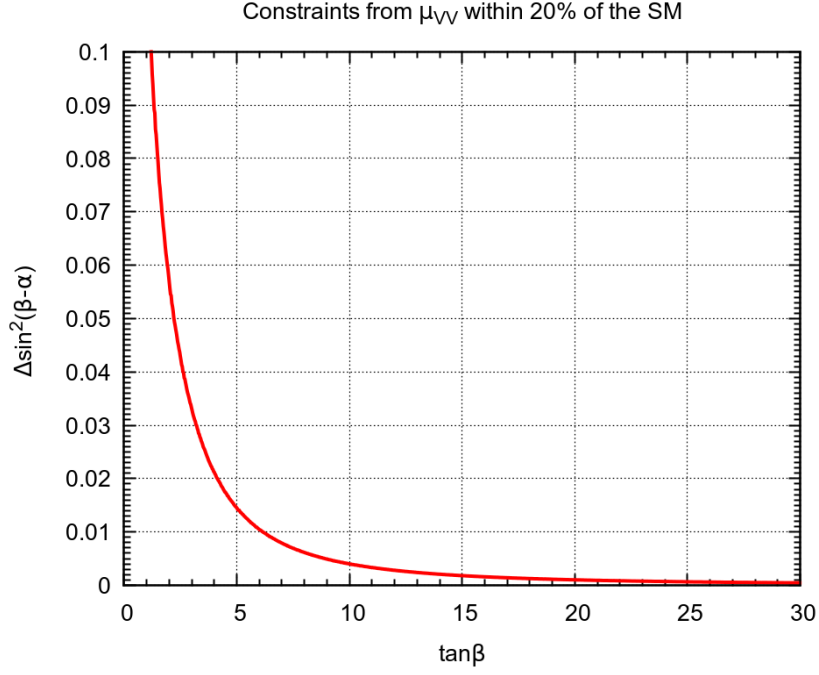


FIG. 3: Fractional variation of $\sin^2(\beta - \alpha)$ as a function of $\tan\beta$ for all points with $k_D < 0$ that obey Eq. (10) with $0.8 \leq \mu_{VV} \leq 1.2$.

Finally, in the left panel of Fig. 4 we show k_D^2 as a function of $\sin^2(\beta - \alpha)$, under the same assumptions (black). For comparison, we show how this relation becomes more constrained if we require $0.95 \leq \mu_{VV} \leq 1.05$ (cyan/light-gray). To emphasize that the trigonometric relations which result from μ_{VV} in Eq. (10) explain most of the results, we show in the right panel of Fig. 4 the same plot but now with points generated obeying all the model constraints and without the simplifying assumptions that led to Eq. (10). These simple considerations will turn out to be very important in the next section.

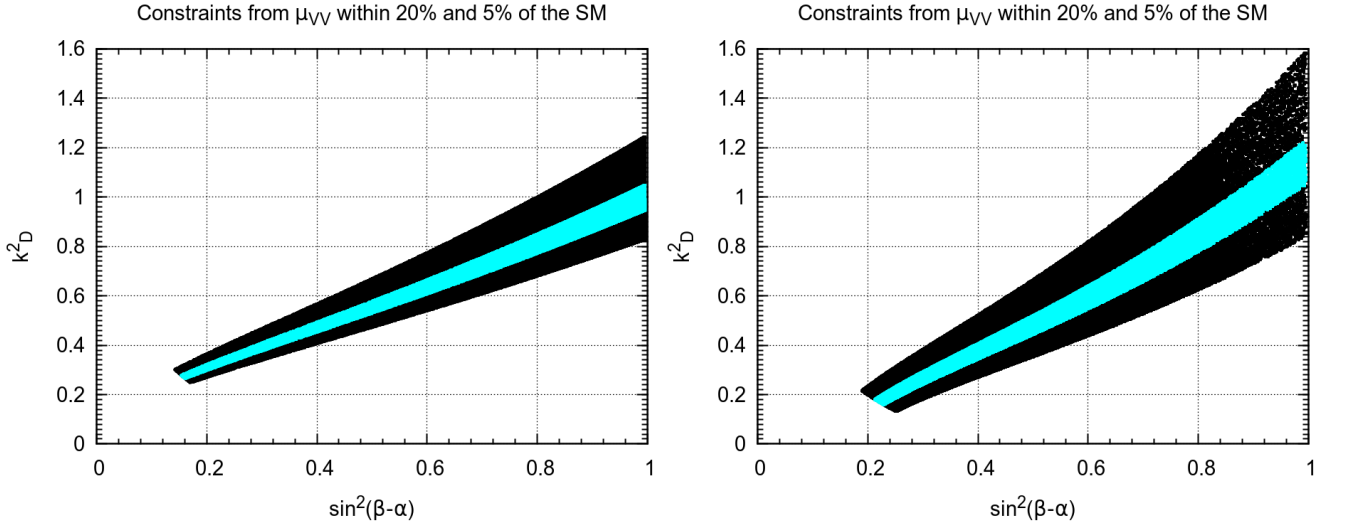


FIG. 4: Left panel: k_D^2 as a function of $\sin^2(\beta - \alpha)$ for all points with $k_D < 0$ that obey Eq. (10) with $0.8 \leq \mu_{VV} \leq 1.2$ (black) or with $0.95 \leq \mu_{VV} \leq 1.05$ (cyan/light-gray). Right panel: The same but for generated data obeying the model constraints.

C. How production affects the rates

In the previous section, we have made a drastic approximation, which reduced the analysis to a simple trigonometric issue in α and β , with no dependence on other 2HDM parameters. Now we resume the SET found by scanning all the 2HDM parameter space and imposing theoretical constraints, as defined at the beginning of section II; we then use all production mechanisms.

In Fig. 5, we show our 8 TeV results for k_D^2 as a function of $\sin^2(\beta - \alpha)$. In black, we see the points generated from the SET, constrained exclusively by $0.8 \leq \mu_{VV} \leq 1.2$. This coincides with the black region in the right panel of

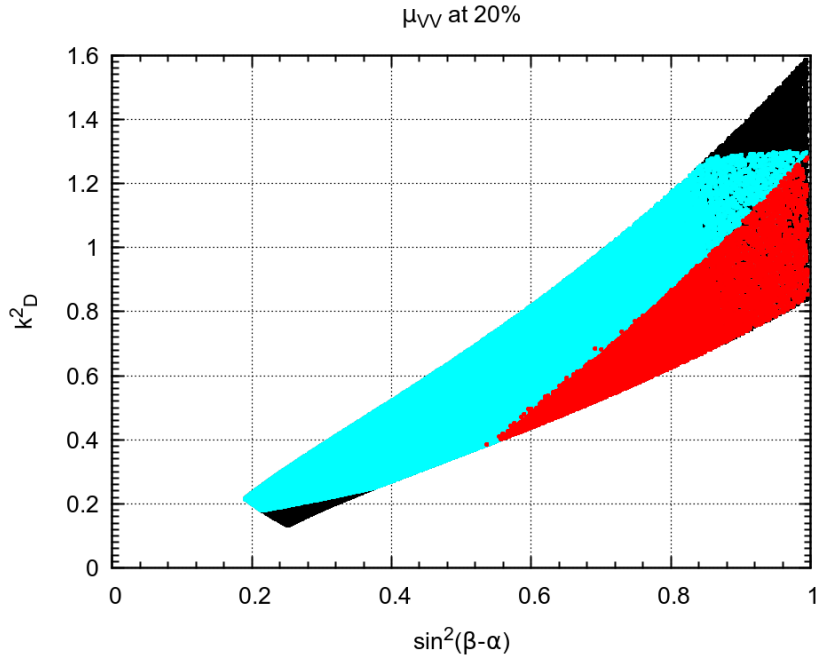


FIG. 5: Allowed region for k_D^2 as a function of $\sin^2(\beta - \alpha)$ for all points with $k_D < 0$ that obey $0.8 \leq \mu_{VV} \leq 1.2$ (black). The region in cyan (light-gray) is obtained by imposing in addition that $0.8 \leq \mu_{\tau\tau} \leq 1.2$, while in the region in red (dark-gray) we further impose $0.8 \leq \mu_{\gamma\gamma} \leq 1.2$.

Fig. 4, and should be compared with the left panel of Fig. 4. As already mentioned, the similarity is uncanny. Simple trigonometry really does have a very strong impact on the results, particularly in the values of $\sin^2(\beta - \alpha)$; its ranges are practically the same in the two figures. The value for k_D^2 for low $\sin^2(\beta - \alpha)$ (which, as we see from the right panel of Fig. 2, occurs for low $\tan\beta$), is also rather similar. There are, of course, minor quantitative differences: some due to the fact that the SET already has some constraints on the model parameters, due to the imposition of the bounded from below, perturbativity and S, T, U conditions; some due to the details of the production mechanism. The most important difference occurs for $\sin^2(\beta - \alpha) \sim 1$ (large $\tan\beta$), where $k_D^2 \sim 1 \pm 0.2$ in Fig. 4, while $k_D^2 \sim 1.2 \pm 0.4$ in Fig. 5. This, as we shall see, is rooted in the production.

It is also interesting to compare Fig. 5, with Fig. 6, which we have drawn using the assumed production rates in Ref. [7]. Notice that the values of k_D^2 are now smaller, especially for $\sin^2(\beta - \alpha) \sim 1$ (large $\tan\beta$).

It is easy to see that imposing further $0.8 \leq \mu_{\tau^+\tau^-} \leq 1.2$ may not make a substantial difference. To understand qualitatively the impact of channels other than $h \rightarrow VV$, let us assume that all observed decays will be measured at the SM rates, with the same error δ . Using Eqs. (6)-(7), we find

$$1 \pm 2\delta \sim \frac{\mu_{f_1}}{\mu_{f_2}} = \frac{R_D^{f_1}}{R_D^{f_2}} \quad (12)$$

for all final states f_1 and f_2 . Notice that this relation does *not* depend on the production rate, nor on the total width

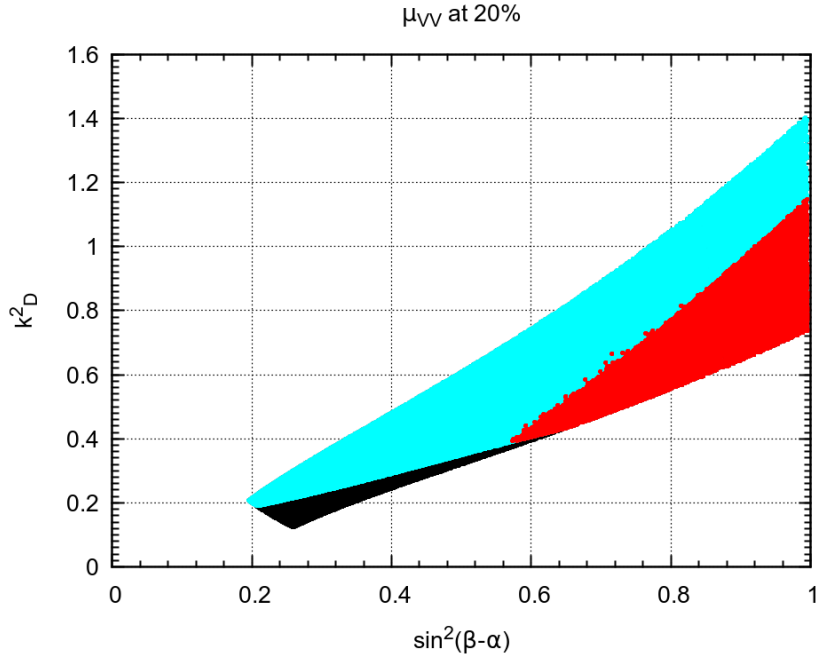


FIG. 6: Same as in Fig. 5, but for the assumed production rates in Ref. [7]. See text for details.

ratios, which are the same for all decays¹. In particular,

$$\frac{\mu_{\tau^+\tau^-}}{\mu_{VV}} = \frac{k_D^2}{\sin^2(\beta - \alpha)}, \quad (13)$$

where we have used Eqs. (2)-(3). This means that, roughly speaking, k_D^2 should lie between the lines $k_D^2 = 0.6 \sin^2(\beta - \alpha)$ and $k_D^2 = 1.4 \sin^2(\beta - \alpha)$, when we consider points which pass current data at around 20%. Close to $\sin^2(\beta - \alpha) \sim 1$, this should reduce the range of k_D^2 from (0.8, 1.6) to, roughly (0.8, 1.4). We did the corresponding simulation (shown in the cyan/light-gray region of Fig. 5) and find roughly (0.8, 1.3). Notice that adding $h \rightarrow b\bar{b}$, assuming that it is produced/measured in all channels with the same 20% error, has no impact, because it would lead to the same Eq. (13). So, we might as well leave it out. Before closing the discussion on the $0.8 < \mu_{\tau^+\tau^-} < 1.2$ cut, let us explain why this has a small effect on Fig. 5, with our production, and has almost no effect on Fig. 6. The reason is that smaller values of k_D^2 also imply that the ratio $\mu_{\tau^+\tau^-}$ is smaller and this explains why most points that passed the μ_{VV} cut at 20% (black) also pass the cut in $\mu_{\tau^+\tau^-}$ (cyan/light-gray). The black points in Fig. 6 are behind the cyan(light-gray) points and only appear for small values of k_D^2 , due to the lower cut on $\mu_{\tau^+\tau^-}$.

Fig. 5 also shows in red/dark-gray the points generated from the SET, and constrained by $0.8 \leq \mu_{\gamma\gamma} \leq 1.2$, in addition to the constraints $0.8 \leq \mu_{VV} \leq 1.2$ and $0.8 \leq \mu_{\tau^+\tau^-} \leq 1.2$. Thus, the combination of VV , $\tau^+\tau^-$, and $\gamma\gamma$ constraints forces $\sin^2(\beta - \alpha) > 0.5$. We recall that, from $h \rightarrow VV$ alone, $\sin^2(\beta - \alpha) \sim 1$ for $\tan\beta > 10$, with a minute spread.

We now turn to a qualitative understanding of the impact of the differing production rates in Figs. 5 and 6. If all production occurred through gluon fusion with an intermediate top, then the answer would be that an increase in production rates would have no impact at all, because it would cancel in Eq. (7), and we would still have $R_P = k_U^2$. In the SM, the production is indeed dominated by gluon fusion with an intermediate top. But, for the gluon fusion in the 2HDM, the interference with an intermediate bottom becomes important. Indeed, let us write

$$\sigma^{2\text{HDM}}(gg \rightarrow h) = k_U^2 g_{tt} + k_U k_D g_{tb} + k_D^2 g_{bb}, \quad (14)$$

where $g_{bb} \ll |g_{tb}| \ll g_{tt}$. In the SM, $k_U = k_D = 1$, and $\sigma^{\text{SM}}(gg \rightarrow h) \sim g_{tt}$. Thus, assuming that all production goes

¹ Except $b\bar{b}$, if we consider that it is only measured in associated production.

through gluon fusion, we find from Eq. (7)

$$R_P \sim k_U^2 \left[1 + \frac{k_D}{k_U} \frac{g_{tb}}{g_{tt}} \right]. \quad (15)$$

where we have neglected g_{bb} (we have verified that this is indeed a very good approximation). This equation has many features that one would expect. If the interference is very small, $k_D g_{tb}/(k_U g_{tt}) \ll 1$, and we recover $R_P \sim k_U^2$, as mentioned above. If one were to increase g_{tb} and g_{tt} by the same multiplicative factor, then R_P would not be altered. So, what is crucial in the difference between Figs. 5 and 6 is that the mix of g_{tb} and g_{tt} has been altered between the simulations, with $|g_{tb}|/g_{tt}$ becoming larger with the production rates used in this article. This is more important for large values of

$$\frac{k_D}{k_U} = -\tan \alpha \tan \beta \sim -\sqrt{\frac{\sin^2(\beta - \alpha)}{\mu_{VV}}}. \quad (16)$$

The approximation at the end would hold if we were to keep the assumptions of section II B. The first equality in Eq. (16) would lead us to believe that the second term in Eq. (15) is much more important as $\tan \beta$ increases. However, this is mitigated by the fact that, as the analysis in section II B and the approximation at the end of Eq. (16) show, k_D/k_U is tied to $\sin^2(\beta - \alpha)/\mu_{VV}$. Indeed, the right panel of Fig. 1, obtained with a full simulation, shows that there are effects of differing production rates as low as $\tan \beta \sim 1$. Before proceeding, it is useful to stress this point. The intuition gained by looking at the dependence of the couplings on α and β , such as in the first equality in Eq. (16), can be completely altered once some experimental bound is imposed, such as the μ_{VV} seen in the approximation at the end of Eq. (16), because the bound may impose rather nontrivial constraints between α and β . In this case, for each $\tan \beta$, the range of allowed α is correlated and very small.

Having established that R_P is larger in our simulation than in the simulation of Fig. 6, we must now understand its differing impact on $\mu_{\gamma\gamma}$, which is almost the same, and on $\mu_{b\bar{b}}$, which increases.

The crucial point comes from the previous section, where we found that $0.8 \leq \mu_{VV} \leq 1.2$ alone gives a very tight constraint on the possible values of $k_V^2 = \sin^2(\beta - \alpha)$, for a given value of $\tan \beta$. Thus, for fixed $\tan \beta$, if we wish to keep $\mu_{VV} = R_P k_V^2 R_{TW}$ constant and close to one, we must always keep $R_P R_{TW} \simeq \text{constant}$. As a result, the only way to accommodate an increased production is to have a decreased R_{TW} (which is roughly determined by $1/k_D^2$), and to increase k_D^2 . This explains why k_D^2 is larger when we use the larger $|g_{tb}|/g_{tt}$, as in Fig. 5, than it is when we use the smaller production $|g_{tb}|/g_{tt}$, as in Fig. 6. Since k_D^2 appears in both $h \rightarrow b\bar{b}$ and $h \rightarrow \tau^+\tau^-$, both are increased in our simulation.

If we were to take the right panel of Fig. 1 at face value, we might have been led to conclude that a measurement $0.9 \leq \mu_{b\bar{b}} \leq 1.1$ or $0.9 \leq \mu_{\tau^+\tau^-} \leq 1.1$ would already exclude the $k_D < 0$ solution for large $\tan \beta$, as can be seen in the right panel of Fig. 1 (red/dark-gray region). Unfortunately, as we have shown, these rates are extremely sensitive to the production and, thus, cannot be used to exclude $k_D < 0$.

In contrast, because, for fixed $\tan \beta$, μ_{VV} implies roughly that $R_P R_{TW} \simeq \text{constant}$, $\mu_{\gamma\gamma}$ is virtually independent of the production and only depends on the decay rate $h \rightarrow \gamma\gamma$. As the largest contribution to this decay comes from the W boson diagrams, and this coupling is already fixed by μ_{VV} , $\mu_{\gamma\gamma}$ will be rather insensitive to the QCD corrections in the production and can be used to constrain $k_D < 0$. As a result, our prediction for $\mu_{\gamma\gamma}$ in the right panel of Fig. 1 mirrors that in Fig. 5-Left of Ref. [7].

The black points in the right panel of Fig. 1 represent the allowed region for $\mu_{\gamma\gamma}$ when we take $0.95 \leq \mu_{VV} \leq 1.05$. As the highest value for this range is only slightly above 0.9, we agree with the conclusion of Ref. [7] that a putative 5% measurement of $h \rightarrow \gamma\gamma$ at 8 TeV around the SM value would rule out $k_D < 0$.

In summary, the constraint $R_P R_{TW} \simeq \text{constant}$ means that, when we increase the $|g_{tb}|/g_{tt}$ mix in the production rates, $\mu_{\gamma\gamma}$ will stay the same², as we have found in Fig. 1. In contrast, since an increased production implies an increased k_D^2 , we find that $\mu_{b\bar{b}} = \mu_{\tau^+\tau^-} = R_P k_D^2 R_{TW} \simeq \text{constant}$ k_D^2 must increase, in accordance with what we see in the same figure.

There are three points to note. First, the next LHC run will occur at 14 TeV, while the current data exists for 8 TeV. Second, the same argument that showed that $\mu_{\gamma\gamma}$ is stable against changes in production can be applied to $\mu_{Z\gamma}$. Third, the same delayed decoupling effect found in $\mu_{\gamma\gamma}$ appears in $\mu_{Z\gamma}$. We address these issues in the next section.

² And, indeed, $\mu_{Z\gamma}$.

III. PREDICTIONS FOR THE 14 TEV RUN

Strictly speaking, future LHC experiments will be carried out at 14 TeV. Moreover, the dominant gluon fusion process shifts by almost a factor of 2.5 in going from 8 to 14 TeV. Naively, when $\tan\beta$ becomes large, the interference between the dominant gluon fusion through a top triangle and the gluon fusion through a bottom triangle becomes important, and then the sign of k_D is crucial. However, as we have already pointed out, things are complicated by the fact that k_D/k_U is tied to $\sin^2(\beta - \alpha)/\mu_{VV}$, and current experiments keep $\sin^2(\beta - \alpha) > 0.5$. Moreover, in gluon fusion, the magnitude squared of the top triangle, the magnitude squared of the bottom triangle, and the interference are multiplied by almost the same factor as one goes from 8 to 14 TeV. As a result, most points that only differ from the SM model measurements by, say, 20% at 8 TeV will also differ from the SM model measurements by 20% at 14 TeV, when we use our production based on the current version of HIGLU with specific PDF's and energy scales. We have performed a simulation with 146110 points to test this issue. Only 800 of those (around 0.6%), pass the 20% test at 8 TeV but not at 14 TeV. So, the conclusions are unaffected by this issue.

In any case, we perform here the following analysis. We first find points (satisfying the conditions in the SET) which differ from the SM at 8 TeV by 20%. Then, we use those 2HDM points to generate all rates at 14 TeV. Our subsequent discussions of the μ parameters and, in particular, on the impact of $h \rightarrow Z\gamma$, are only based on the surviving points.

Assuming current experiments (20% errors at 8 TeV), our predictions for $\mu_{\tau^+\tau^-}$ (in red/dark-gray) and $\mu_{\gamma\gamma}$ (in black) are shown on the left panel of Fig. 7. We see that, at this level of precision, we cannot rule out the $k_D < 0$

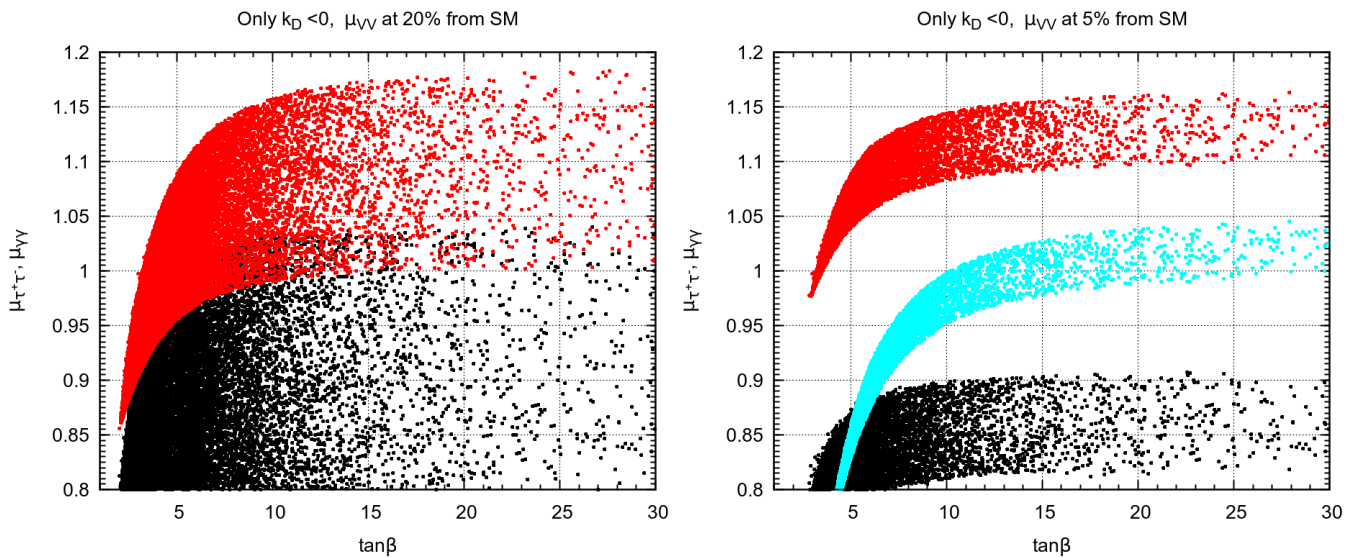


FIG. 7: Left panel: Prediction for $\mu_{\tau^+\tau^-}$ (red/dark-gray) and $\mu_{\gamma\gamma}$ (black) as a function of $\tan\beta$ for the LHC at 14 TeV with the constraint of 20% errors at 8 TeV. Right panel: Assuming now that μ_{VV} are within 5% of the SM prediction at 14 TeV, we plot the same quantities. Also shown (cyan/light-gray) is the prediction for $\mu_{b\bar{b}}(Vh)$ from associated production.

branch.

If we now imagine that, in addition, the μ_{VV} are measured at 14 TeV to lie around unity with a 5% precision, then we obtain for $\mu_{\tau^+\tau^-}$ (in red/dark-gray) and $\mu_{\gamma\gamma}$ (in black) in the right panel of Fig. 7. Here, we would be led to conclude that a 5% measurement of $\mu_{\tau^+\tau^-} \sim 1$ would exclude $k_D < 0$ for large $\tan\beta$. As explained in the previous section, this conclusion is misleading since the $\mu_{\tau^+\tau^-}$ (and the $\mu_{b\bar{b}}$ rates, combining all production modes) depend crucially on the detailed mix of the gluon production through intermediate tops and bottoms. Thus, we agree with Ref. [7] that a 5% measurement of $\mu_{\gamma\gamma}$ can be used to exclude the wrong-sign solution, while $\mu_{\tau^+\tau^-}$ should not.

We recall that the $\mu_{b\bar{b}}$ we present (in red/dark-gray) in Fig. 1 was calculated assuming that $b\bar{b}$ is measured in all channels, and using our production rates. In that case, it would seem that a 5% of $\mu_{b\bar{b}}$ could exclude $k_D < 0$. However, as with $\mu_{\tau^+\tau^-}$, the result is very sensitive to the production, and, thus, cannot be used to probe $k_D < 0$. In foreseeing the 14 TeV run, we differ from Ref. [7], and study $b\bar{b}$ only in the Vh production channel, shown in cyan/light-gray on the right panel of Fig. 7. Unfortunately, in contrast with what happens with our $\mu_{b\bar{b}}$ in Fig. 1, a 5% measurement of $\mu_{b\bar{b}}(Vh)$ is centered around unity for $\tan\beta > 10$, and, thus, it cannot be used to preclude $k_D < 0$.

We now turn our attention to the decay $h \rightarrow Z\gamma$. As mentioned above, there are three good reasons to look at this decay. First, the decay will be probed at LHC's Run2, and there are already upper bounds on it from Run1.

Second, as for $\mu_{\gamma\gamma}$, we did not find a significant difference when using different production rates. Third, the delayed decoupling that has been used in showing the usefulness of a future measurement of $\mu_{\gamma\gamma}$ is also present in $\mu_{Z\gamma}$. The expressions for this decay can be found in Ref. [8], which we have checked.

Starting from the SET, we calculated μ for VV , $\gamma\gamma$, and $\tau^+\tau^-$ at 8 TeV, requiring that all lie within 20% of the SM. The remaining points were required to pass μ_{VV} , within 5% of the SM, at 14 TeV. We then calculated $\mu_{Z\gamma}$, $\mu_{\tau^+\tau^-}$ and $\mu_{\gamma\gamma}$. Our results are shown in Fig. 8. There are bad news and good news.

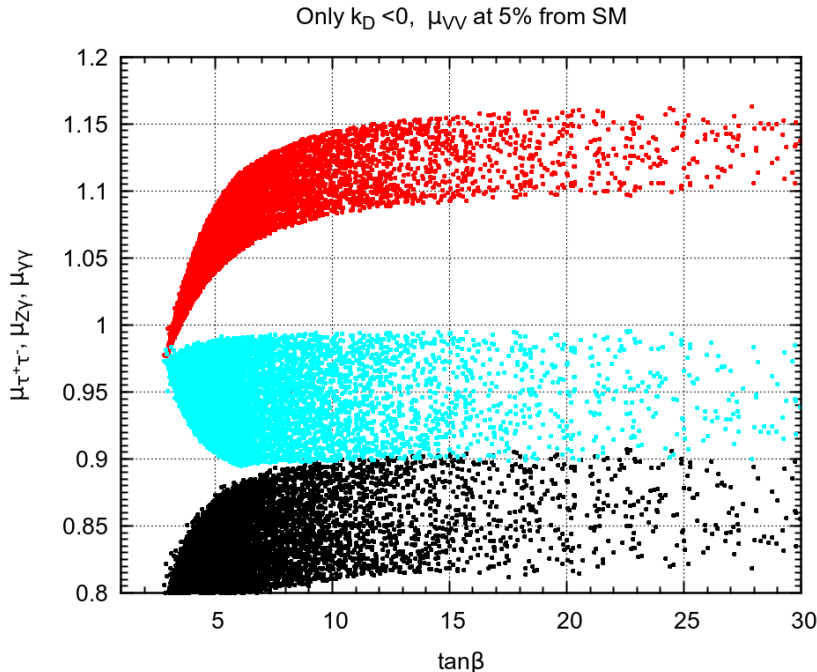


FIG. 8: Prediction for $\mu_{\tau^+\tau^-}$ (red/dark-gray), $\mu_{Z\gamma}$ (cyan/light-gray) and $\mu_{\gamma\gamma}$ (black) as a function of $\tan\beta$, for the LHC at 14 TeV, with a measurement of μ_{VV} within 5% of the SM at 14 TeV.

The bad news comes from the fact that the results in Fig. 8 show that $\mu_{Z\gamma} \lesssim 1$. Therefore, this channel cannot be used to exclude the $k_D < 0$ solution. The good news are the following. The ratio μ_{VV} , even at 20%, puts a strong bound on $\mu_{Z\gamma}$. In fact, we found that, for $k_D < 0$ and before applying the μ_{VV} constraint, $\mu_{Z\gamma}$ could be as large as two for $\mu_{\gamma\gamma} \sim 1$, as shown in the black region of Fig. 9. However, the requirement that μ_{VV} should be within 20% of the SM drastically limits this upper bound, requiring it to be very close to the SM value, as shown in the red/dark-gray region of Fig. 9. If we require a measurement of μ_{VV} to be within 5% of the SM (cyan/light-gray region of Fig. 9), then both $\mu_{\gamma\gamma}$ and $\mu_{Z\gamma}$ have to be below their SM values for $k_D < 0$. We find that this effect is more predominant in $\gamma\gamma$ ($\mu_{\gamma\gamma} < 0.9$) than in $Z\gamma$ ($\mu_{Z\gamma} < 1$).

Having discussed what we can learn from $\mu_{\gamma\gamma}$ and $\mu_{Z\gamma}$ for the wrong-sign branch, $k_D < 0$, we can ask what is the situation with the *normal* branch, $k_D > 0$. This is shown in Fig. 10. We see that even before requiring any constraint on μ_{VV} (black points), there is only a very small region with large $\mu_{Z\gamma}$ which is compatible with $0.8 \leq \mu_{\gamma\gamma} \leq 1.2$ from current LHC data. In particular, points from the SET, with $\mu_{\gamma\gamma} \sim 1$ and $\mu_{Z\gamma} \sim 2$, allowed for $k_D < 0$ in the black region of Fig. 9, are almost forbidden for $k_D > 0$ in the black region of Fig. 10. If we further require μ_{VV} to be within 20% (red/dark-gray) or 5% (cyan/light-gray) both $\mu_{\gamma\gamma}$ and $\mu_{Z\gamma}$ have to be close to the SM values, with a wider range allowed for $\mu_{\gamma\gamma}$.

We conclude that, for both signs of k_D , current bounds on μ_{VV} already preclude a value of $\mu_{Z\gamma} > 1.5$ from being compatible with the usual 2HDM with softly broken Z_2 . A measurement in the next LHC run of μ_{VV} lying within 5% of the SM will essentially force $\mu_{Z\gamma} \lesssim 1$ for $k_D < 0$ and $\mu_{Z\gamma} \lesssim 1.05$ for $k_D > 0$.

IV. PREDICTIONS FOR THE FLIPPED 2HDM

In this section, we analyze the Flipped 2HDM. This coincides with the Type II 2HDM, except that the charged leptons couple to the Higgs proportionally to k_U (not k_D).

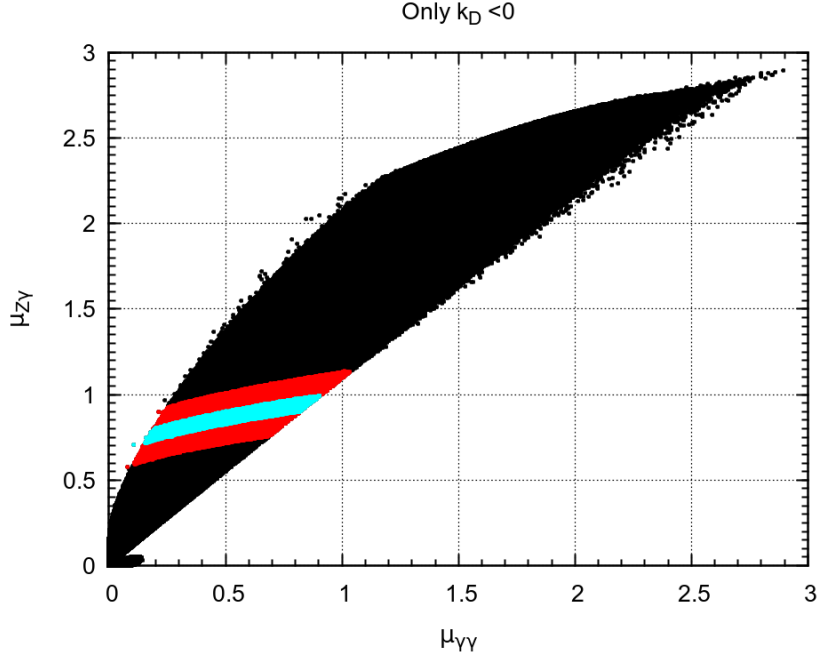


FIG. 9: Predictions for $\mu_{Z\gamma}$ versus $\mu_{\gamma\gamma}$ at 14 TeV, for $k_D < 0$. In black, we have the points in the SET (obeying theoretical constraints and S, T, U , only). In red/dark-gray (cyan/light-gray), the points satisfying in addition VV within 20% (5%) of the SM, at 14 TeV.

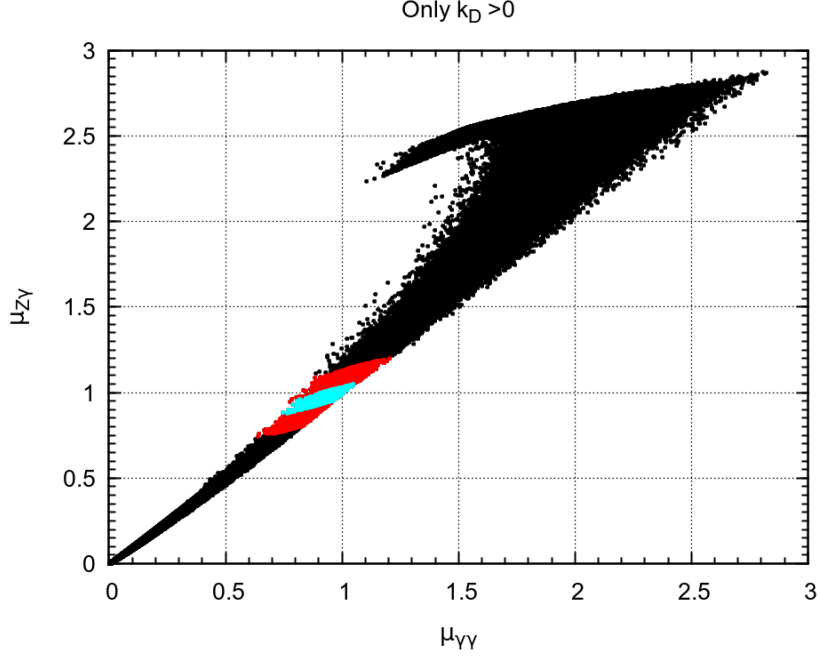


FIG. 10: Predictions for $\mu_{Z\gamma}$ versus $\mu_{\gamma\gamma}$ at 14 TeV, for $k_D > 0$. In black, we have the points in the SET (obeying theoretical constraints and S, T, U , only). In red/dark-gray (cyan/light-gray), the points satisfying in addition VV within 20% (5%) of the SM, at 14 TeV.

We recall that $\mu_{\tau^+\tau^-}$ does not have a big effect in Fig. 5, for the Type II 2HDM. This has a simple explanation, through the approximation in Eq. (13). In the Flipped 2HDM, the same approximation yields

$$\frac{\mu_{\tau^+\tau^-}}{\mu_{VV}} = \frac{k_U^2}{\sin^2(\beta - \alpha)}, \quad (17)$$

leading one to suspect that $\mu_{\tau^+\tau^-}$ might have a larger effect here. This is confirmed in the left panel of Fig. 11, where we show our 8 TeV results for k_D^2 as a function of $\sin^2(\beta - \alpha)$. The colour codes, explained in the figure caption,

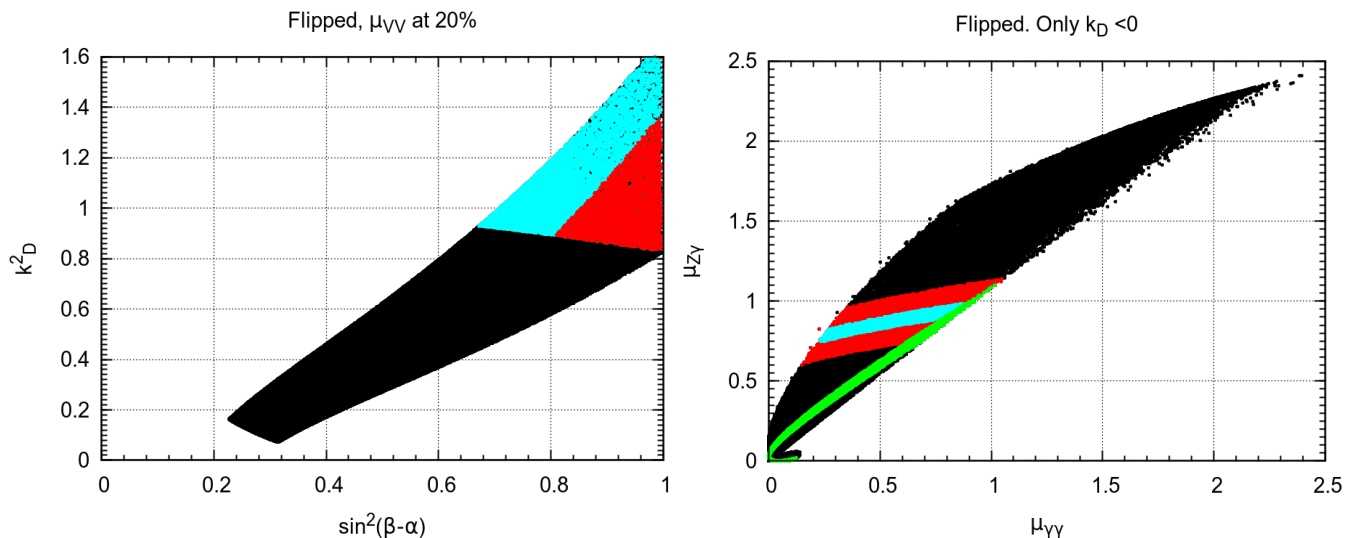


FIG. 11: Left panel: Allowed region for k_D^2 as a function of $\sin^2(\beta - \alpha)$ in the Flipped 2HDM, for all points with $k_D < 0$ that obey $0.8 \leq \mu_{VV} \leq 1.2$ (black). The region in cyan (light-gray) is obtained by imposing in addition that $0.8 \leq \mu_{\tau\tau} \leq 1.2$, while in the region in red (dark-gray) we further impose $0.8 \leq \mu_{\gamma\gamma} \leq 1.2$. Right panel: Predictions for $\mu_{Z\gamma}$ versus $\mu_{\gamma\gamma}$ at 14 TeV, for $k_D < 0$, in the Flipped 2HDM. In black, we have the points in the SET (obeying theoretical constraints and S, T, U , only). In red/dark-gray (cyan/light-gray), the points satisfying in addition VV within 20% (5%) of the SM, at 14 TeV. Shown in green/light-gray are the points satisfying $\mu_{\tau^+\tau^-}$ at 20% of the SM, which lie on a line going diagonally from the origin with almost unit slope.

mirror those in Fig. 5. Here the 20% measurement of $\mu_{\tau^+\tau^-}$ does have a big impact.

However, one might suspect that this may not change much the conclusions on $\gamma\gamma$ and $Z\gamma$, because, as mentioned before, those were primarily determined by the constraint on μ_{VV} . This is what we find in the right panel of Fig. 11. The effect of $\mu_{\tau^+\tau^-}$ is to reduce the allowed region by a very fine slice, shown in the right panel of Fig. 11 as a green/light-gray line going diagonally from the origin with almost unit slope. This figure should be compared with Fig. 9, which holds in the Type II 2HDM. In both cases, a 5% measurement of $\mu_{\gamma\gamma}$ ($\mu_{Z\gamma}$) will (will not) exclude $k_D < 0$.

V. CONCLUSIONS

We have analysed the Type II 2HDM with softly broken Z_2 , scrutinizing the possibility that the $hb\bar{b}$ coupling has a sign opposite to that in the SM and the impact on this issue of $Z\gamma$. We impose the usual theoretical constraints, assuming that μ_{VV} , $\mu_{\tau^+\tau^-}$, and $\mu_{\gamma\gamma}$ differ from the SM by no more than 20% at 8 TeV. We found that the constraint from μ_{VV} is crucial, and can be understood in simple trigonometric terms. In particular, we show that this cut has a rather counter-intuitive implication. Before this cut is applied, it would seem that the importance of the bottom-mediated gluon fusion production mechanism would grow linearly with $\tan\beta$. However, after current bounds are placed on μ_{VV} , the importance of the bottom-mediated gluon fusion production mechanism grows asymptotically into a constant, for large $\tan\beta$. This generalizes as a cautionary tale: applying a new experimental bound may force unexpected relations among the parameters, and the theoretical intuition must be revised in this new framework.

In projecting to the future, we have then simulated our points at 14 TeV, highlighting the fact, for the issues that interest us, using the current version of HIGLU at 14 TeV or at 8 TeV leads to the same results. We have shown that results for the $b\bar{b}$ and $\tau^+\tau^-$ depend sensitively on the ratio g_{tb}/g_{tt} encoding the relative weight of the square of the top-mediated gluon fusion production amplitude, and the interference of this amplitude with the bottom-mediated gluon fusion production amplitude. As a result, these channels should not be used to probe the $k_D < 0$ possibility. Even if that were not the case, since $b\bar{b}$ is only measured in associated production and, as we show, $\mu_{b\bar{b}}(Vh)$ includes unity, this channel would not be useful.

In contrast, in our simulations both $\gamma\gamma$ and $Z\gamma$ are roughly independent of g_{tb}/g_{tt} . In addition, they exhibit delayed decoupling in the hH^+H^- vertex. As a result, they could, in principle, be used to probe the $k_D < 0$ possibility. Indeed,

as found in Ref. [7], a 5% measurement of $\mu_{\gamma\gamma}$ around unity will be able to exclude $k_D < 0$.

We then performed a detailed analysis of $Z\gamma$. We show that, before including the LHC data, values of $\mu_{\gamma\gamma}$ and $\mu_{Z\gamma}$ were allowed between 0 and 3, but with a correlation between the two, as shown in the black regions of Fig. 9 and Fig. 10. This correlation is more important (that is, the region in the figure is smaller) for $k_D > 0$ than it is for $k_D < 0$. In particular, $\mu_{\gamma\gamma} \sim 1$ with $\mu_{Z\gamma} \sim 2$ would be possible in the latter case, but not in the former. Things change dramatically when the simple constraint $0.8 < \mu_{VV} < 1.2$ is imposed. In that case, we obtain the red/dark-gray regions of Fig. 9 ($k_D < 0$) and Fig. 10 ($k_D > 0$). This already places $\mu_{\gamma\gamma}$ and $\mu_{Z\gamma}$ close to the SM, although, strictly speaking, points with $\mu_{\gamma\gamma} = 1$ with $\mu_{Z\gamma} = 1$ are not allowed in our simulation when $k_D < 0$. A 5% measurement of VV around the SM at 14 TeV will bring $\mu_{Z\gamma}$ closer to unity, for $k_D > 0$, and just below unity, for $k_D < 0$. Thus, this decay cannot be used to exclude $k_D < 0$.

But we have the reverse advantage. It is obvious that a measurement of $\mu_{Z\gamma} > 1$ would exclude the SM. We have shown that a 5% precision on μ_{VV} around the SM, together with $\mu_{Z\gamma} > 1$, would also exclude $k_D < 0$, and, together with $\mu_{Z\gamma} > 1.1$, would exclude altogether the Type II 2HDM with softly broken Z_2 . If $\mu_{Z\gamma}$ turns out to lie a mere 20% above the SM value, then the softly broken Type II 2HDM is not the solution.

Finally, we analyzed the Flipped 2HDM. Although there is a substantial difference in the k_D^2 versus $\sin^2(\beta - \alpha)$ plane, this does not change dramatically the $\mu_{\gamma\gamma}$ - $\mu_{Z\gamma}$ correlation. As a result, here 5% measurements of VV and $\gamma\gamma$ around the SM at 14 TeV will be enough to exclude $k_D < 0$, while $\mu_{Z\gamma}$ will not.

Acknowledgments

We are grateful to Rui Santos for many discussions related to the Higgs production channels and to the work [7]. This work was partially supported by FCT - *Fundação para a Ciência e a Tecnologia*, under the projects PEst-OE/FIS/UI0777/2013 and CERN/FP/123580/2011. D. F. is also supported by FCT under the project EXPL/FIS-NUC/0460/2013.

-
- [1] G. Aad *et al.* [ATLAS Collaboration], Phys. Lett. B **716**, 1 (2012) [arXiv:1207.7214 [hep-ex]].
 - [2] S. Chatrchyan *et al.* [CMS Collaboration], Phys. Lett. B **716**, 30 (2012) [arXiv:1207.7235 [hep-ex]].
 - [3] Up to date results can be found in ATLAS Collaboration, <https://twiki.cern.ch/twiki/bin/view/AtlasPublic/HiggsPublicResults>; and in CMS Collaboration, <https://twiki.cern.ch/twiki/bin/view/CMSPublic/PhysicsResultsHIG>.
 - [4] D. Carmi, A. Falkowski, E. Kuflik and T. Volansky, JHEP **1207**, 136 (2012) [arXiv:1202.3144 [hep-ph]].
 - [5] C. -W. Chiang and K. Yagyu, JHEP **1307**, 160 (2013) [arXiv:1303.0168 [hep-ph]].
 - [6] A. Barroso, P. M. Ferreira, R. Santos, M. Sher and J. P. Silva, arXiv:1304.5225 [hep-ph], talk given by R. Santos at Toyama International Workshop on Higgs as a Probe of New Physics (13-16, February, 2013).
 - [7] P. M. Ferreira, J. F. Gunion, H. E. Haber and R. Santos, arXiv:1403.4736 [hep-ph].
 - [8] J. F. Gunion, H. E. Haber, G. L. Kane and S. Dawson, "The Higgs Hunter's Guide," Front. Phys. **80**, 1 (2000).
 - [9] G. C. Branco, P. M. Ferreira, L. Lavoura, M. N. Rebelo, M. Sher and J. P. Silva, Phys. Rept. **516**, 1 (2012) [arXiv:1106.0034 [hep-ph]].
 - [10] P. Posch, Phys. Lett. B **696**, 447 (2011) [arXiv:1001.1759 [hep-ph]].
 - [11] N. D. Christensen and C. Duhr, Comput. Phys. Commun. **180**, 1614 (2009), [arxiv:0806.4194].
 - [12] A. Arhrib, M. Capdequi Peyranere, W. Hollik and S. Penaranda, Phys. Lett. B **579**, 361 (2004) [hep-ph/0307391].
 - [13] G. Bhattacharyya, D. Das, P. B. Pal and M. N. Rebelo, JHEP **1310**, 081 (2013) [arXiv:1308.4297 [hep-ph]].
 - [14] S. Chatrchyan *et al.* [CMS Collaboration], Phys. Rev. D **89**, 012003 (2014) [arXiv:1310.3687 [hep-ex]].
 - [15] B. Tuchming, (for the CDF and D0 Collaborations) arXiv:1405.5058 [hep-ex].
 - [16] G. Aad *et al.* [ATLAS Collaboration], Phys. Lett. B **732**, 8 (2014) [arXiv:1402.3051 [hep-ex]].
 - [17] S. Chatrchyan *et al.* [CMS Collaboration], Phys. Lett. B **726**, 587 (2013) [arXiv:1307.5515 [hep-ex]].
 - [18] N. G. Deshpande and E. Ma, Phys. Rev. D **18**, 2574 (1978).
 - [19] S. Kanemura, T. Kubota and E. Takasugi, Phys. Lett. B **313**, 155 (1993) [hep-ph/9303263].
 - [20] A. G. Akeroyd, A. Arhrib and E. -M. Naimi, Phys. Lett. B **490**, 119 (2000) [hep-ph/0006035].
 - [21] I. F. Ginzburg and I. P. Ivanov, hep-ph/0312374.
 - [22] W. Grimus, L. Lavoura, O. M. Ogreid and P. Osland, Nucl. Phys. B **801**, 81 (2008) [arXiv:0802.4353 [hep-ph]].
 - [23] M. Baak, M. Goebel, J. Haller, A. Hoecker, D. Kennedy, R. Kogler, K. Moenig and M. Schott *et al.*, Eur. Phys. J. C **72**, 2205 (2012) [arXiv:1209.2716 [hep-ph]].
 - [24] M. Spira, hep-ph/9510347.
 - [25] R. V. Harlander, S. Liebler and H. Mantler, Computer Physics Communications **184**, 1605 (2013) [arXiv:1212.3249 [hep-ph]].
 - [26] <https://twiki.cern.ch/twiki/bin/view/LHCPhysics/CrossSectionsFigures>.
 - [27] P. M. Ferreira, R. Santos, H. E. Haber and J. P. Silva, Phys. Rev. D **87**, 055009 (2013) [arXiv:1211.3131 [hep-ph]].